Contemporary Mathematics
https://ojs.wiserpub.com/index.php/CM/

Research Article

Thermal Performance of Williamson Fluid Flow over Vertical Stretching Sheet: A Mathematical and Machine Learning Perspective

Nadeem Abbas[1*], Wasfi Shatanawi[1], Fady Hasan[1], Lubaba Yaseen[2]

[1] Department of Mathematics and Sciences, College of Humanities and Sciences, Prince Sultan University, Riyadh, 11586, Saudi Arabia
[2] Department of Mathematics, Riphah International University Faisalabad Campus, Main Satyana Road, Faisalabad, 44000, Pakistan
E-mail: nabbas@psu.edu.sa

Received: 20 July 2025; **Revised:** 11 November 2025; **Accepted:** 11 November 2025

Abstract: Stagnation flow of Williamson fluid over nonlinearly stretching vertical sheet with heat generation, viscous dissipation and thermal slip has been analyzed. Governing equations have been formulated using boundary layer approximation and expressed as differential equations. Then, we transformed into dimensionless form through suitable similarity variables. Applying the boundary layer approximation, the governing Partial Differential Equations (PDEs) have been transformed into Ordinary Doifferential Equatiuons (ODEs). Hybrid techniques has been adopted which combined the numerical technique and Artificial Neural Networks (ANN) to enhance prediction and analysis. Results have indicated that governing parameters have strongly influenced flow and heat transfer characteristics, while ANN predictions have accurately validated numerical outcomes. The integrated approach has demonstrated the capability of ANN in complementing numerical simulations for complex fluid dynamics systems. Effects of key physical parameters have been illustrated through graphs and tables, showing that an increasing Grashof number has strengthened buoyancy-driven flow and enhanced fluid motion near the surface. Response Surface Methodology (RSM) is presented and sensitivity of Nusselt number in relation with various parameters is discussed in detail.

***Keywords*:** vertical variable stretching sheet, Williamson fluid, artificial neural network

MSC: 76A05, 00A69, 37N30, 65L10

Nomenclature

B_0	Magnetic field strength $(\mathrm{N\,m\,A^{-1}})$	$(c_p)_f$	Heat capacity $(\mathrm{J/m^3\,K})$
U_e	Free stream velocity $(\mathrm{m/s})$	α_f	Thermal diffusivity $(\mathrm{m^2/s})$
ν_f	Kinematic viscosity $(\mathrm{m^2/s})$	U_w	Wall velocity
σ	Electric conductivity	γ	Stretching rate
T_∞	Ambient temperature (K)	B	Rate of stretching
Rd	Thermal radiation	Pr	Prandtl number
μ_f	Dynamic viscosity $(\mathrm{kg/(ms)})$	M	Magnetic field
Q	Heat generation	T	Fluid temperature (K)
Sc	Schmidt number	U, V	Velocity components $(\mathrm{m/s})$

Copyright ©2026 Nadeem Abbas, et al.
DOI: https://doi.org/10.37256/cm.7220267909
This is an open-access article distributed under a CC BY license
(Creative Commons Attribution 4.0 International License)
https://creativecommons.org/licenses/by/4.0/

Re_x	Local Reynolds number	Γ	Positive time constant
Θ	Dimensionless temperature	F	Dimensionless stream function
X, Y	Coordinates (Cartesian)	τ	Extra stress tensor $(\mathrm{N/m^2})$
C_f	Skin friction	Nu_x	Nusselt number
λ_1	Thermal slip	λ	Williamson parameter

1. Introduction

Heat transfer and boundary layer flow over stretching sheet play a vital role in real-world problems because of a wide range of uses such as paper production, food manufacturing, wire drawing, extrusion of polymer, production of glass fiber plastic films stretching and so on. Sakiadis [1] initiated the study of boundary layer flow over continuous flat surface. Crane [2] extended the work of Sakiadis [1] by considering flow over a stretching plate. Mahapatra and Gupta [3] discussed the results of stagnation flow at a stretching sheet. Sharma et al. [4] investigated the effects of a heat source or sink on Magnetohydrodynamic (MHD) mixed convective stagnation point flow along a vertical stretching sheet revealing that the heat transfer rate increases with increasing magnetic parameter but decreases as the heat source intensity increases. Mahmood et al. [5] examined the impact of thermal stratification in MHD mixed convective stagnation point flow of nanofluid past a permeable stretching sheet. The authors addressed uncertainties in thermal parameters and how they affect flow and heat transfer characteristics. Recently, numerous authors have studied the influence of physical phenomena on stretching sheets see Refs. [6, 7].

The Williamson model for fluid flow describes a type of non-Newtonian, shear-thinning fluid introduced by Williamson to characterize the behavior of pseudoplastic materials. Unlike Newtonian fluids which keep a constant viscosity regardless of applied shear rate. Williamson fluids show a decrease in effective viscosity as shear rate increases. Their behavior reflects their viscoelastic and shear-thinning properties. The model is very useful for examining complicated industrial processes that involve polymer solutions, suspensions and other materials where traditional Navier-Stokes equations do not accurately describe fluid behavior. Salahuddin et al. [8] analyzed the behavior of Williamson fluid flowing over a stretching sheet with varying thickness and employed numerical methods to explore the effects of magnetic fields and non-conventional heat transfer patterns. Their investigation highlighted the impact of variable sheet geometry and advanced thermal models in accurately predicting flow and heat transfer behaviors. Hamid et al. [9] explored unsteady stagnation point flow of Williamson fluid. Authors have discussed the influence of stretching/shrinking sheet having Ohmic heating. Megahed [10] was the first to investigate the behavior of nonlinear stretching sheet with effects of loss heat and thermal radiation. His study provided valuable visions into temperature distribution and dynamics of boundary layer. Wang et al. [11] examined the influence of MHD effects on Williamson nanofluid flow over thin elastic sheet. Their research highlighted the interactions between magnetic fields, nanoparticle concentration and stability of bioconvection. Botmart et al. [12] enhanced random computational method to address complex model of mass and heat transfer. Several authors have detailed and elaborated non Newtonian models using flow patterns see Refs. [13, 14].

The study of MHD flow and heat transfer in nanofluid has garnered significant attention due to its wide ranging applications in engineering and technology. Early investigations focused on MHD stagnation point flow towards stretching surface discussed by Ishak et al. [15]. The application of machine learning algorithms to assess heat transfer in ternary hybrid nanofluid flow across various geometry which was discussed by Mishra et al. [16]. Nadeem et al. [17] investigated the effects of MHD on nanofluid flow under natural convection and their numerical findings were discussed in detail.

Heat transfer is affected by changes in temperature distributions due to viscous dissipation. The influence of viscous dissipation depends on whether the surface is cooled or heated. Due to lots of applications, few researchers discussed the viscous dissipation should be Due to its numerous applications, several researchers have discussed viscous dissipation. Vajravelu and Hadjinicolaou [18] studied viscous fluid flow with the internal heat generation and viscous dissipations at stretching sheet.

Neural Network Analysis (NNA) is powerful computational approach inspired by structure and functioning of the human brain. It involves using Artificial Neural Networks (ANNs) to model complex relationships between inputs and outputs, identify patterns and make data driven predictions. ANNs comprise interconnected layers of nodes (neurons),

each unit performed basic computations that when integrated allowed network to address complex nonlinear problems across diverse domains. Neural networks have developed for pattern recognition and signal processing. They have since become essential tools in various fields including image classification, natural language processing, time series forecasting and scientific computing. Their ability to learn from large datasets through training processes such as backpropagation and gradient descent makes them particularly suitable for problems where conventional algorithms struggled. As computational resources and algorithms continued to advance neural network analysis is expected to continue play an even more significant role in solving complex data intensive scientific and engineering challenges. Shafiq et al. [19] debated the ANN analysis. Madhu et al. [20] applied multilayer neural networks to investigate three dimensional non Newtonian fluid flow influenced by magnetic and biological factors. Fatima et al. [21] highlighted the careau fluid effect by numerical as well as neural network analysis. Shaheen et al. [22] utilized ANN analysis to examine temperature dependent properties in nanofluid flow over curved surface.

In this paper, we examined the effects of viscous dissipation and heat generation on flow of Williamson fluid over variable stretchable surface. We developed mathematical model to describe the flow behavior over surface. Which was solved using a numerical scheme. The results are presented in both tabular and graphical formats. To enhance the analysis, we employed ANN to model and predict the system behavior. This innovative approach added the numerical solutions and enhanced both accuracy and computational efficiency. The inclusion of ANN underscores the novelty of our study by integrating traditional numerical techniques with modern machine learning frameworks. Our research has potential applications in advanced engineering systems such as polymer processing, biomedical flows and heat transfer devices.

2. Mathematical modeling

Consider the Williamson fluid flow over a vertically stretching surface with viscous dissipation and heat generation. The configuration of the fluid flow over the stretching surface is illustrated in Figure 1. The neural paradigm of the Least Mean Square (LMS) model for second-grade fluid flow is shown in Figure 2. Figure 3 presents the complete flow diagram of the methodology. The stagnation flow along the X direction is considered. The U_∞ and U_w are free stream velocity and stretching sheet. T_w and T_∞ are the wall temperature and ambient temperature. The governing equations are based on the following assumptions:

- Incompressible steady flow in the stagnation region
- Vertical stretching sheet
- Magnetic field
- Williamson fluid flow governed by a boundary value problem
- Viscous dissipation and thermal radiation with slip effects.

The mathematical model under the above assumptions is presented as follows (see Refs. [11, 12]):

$$\frac{\partial}{\partial X}(U)+\frac{\partial}{\partial Y}(V)=0, \tag{1}$$

$$U\frac{\partial U}{\partial X}+\frac{\partial U}{\partial Y}V=\frac{\partial U_e}{\partial X}U_e+\nu_f\left(\frac{\partial^2 U}{\partial Y^2}\right)+\Gamma\sqrt{2}\left(\frac{\partial^2 U}{\partial Y^2}\right)\frac{\partial U}{\partial Y}-\sigma\frac{B_0^2}{\rho_f}(U-U_e)\pm g\beta_T(T-T_\infty) \tag{2}$$

$$U\frac{\partial T}{\partial X}+\frac{\partial T}{\partial Y}V=\alpha_f\left(\frac{\partial^2 T}{\partial Y^2}\right)-\frac{\partial q_r}{\partial Y}+\frac{\mu_f}{(\rho c_p)_f}\left(\frac{\partial U}{\partial Y}\right)\left(\frac{\partial U}{\partial Y}+\frac{\Gamma}{\sqrt{2}}\frac{\partial U}{\partial Y}\frac{\partial U}{\partial Y}\right)+\frac{\sigma}{(\rho c_p)_f}B_0^2U^2+\frac{Q_0}{(\rho c_p)_f}(T-T_w). \tag{3}$$

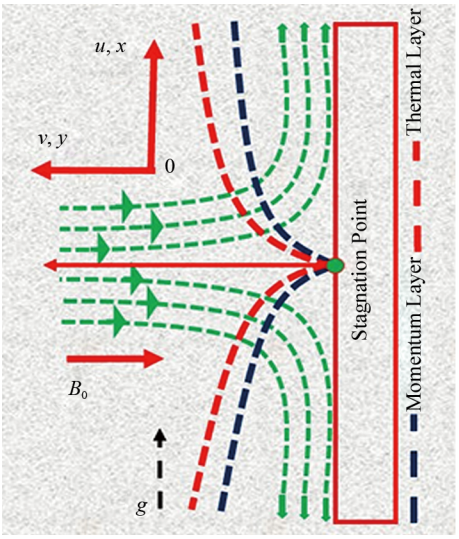


Figure 1. Flow pattern over vertical surface

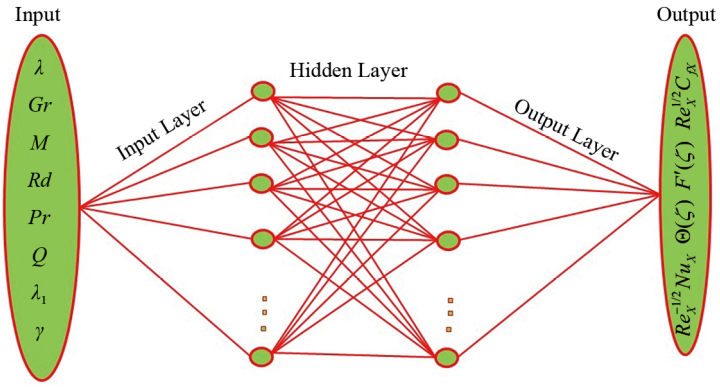


Figure 2. Pattern of neural paradigm

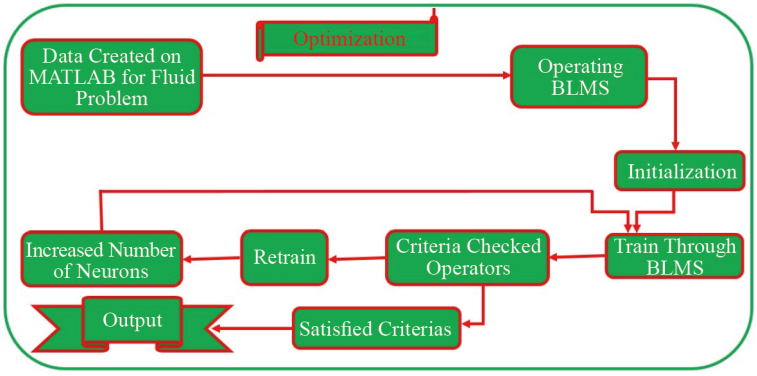


Figure 3. Pattremt of work flow method

The boundary conditions are given by:

$$U = U_w(X),\ V = 0,\ T = T_w + L_1\frac{\partial T}{\partial Y},\ \text{as } Y \to 0,$$
$$U = U_e(X),\ T = T_\infty,\ Y \to \infty. \tag{4}$$

The v_f, ρ_f, and $(c_p)_f$ are specified the kinematics viscosity, density and specific heat. The transformations are offered as:

$$\zeta = \left(B/v_f\right)^{\frac{1}{2}} X^{-\frac{1}{3}} Y,\ U = BX^{\frac{1}{3}} F'(\zeta),\ \Theta(\zeta) = \frac{T - T_\infty}{T_w - T_\infty},$$
$$V = -\left(\sqrt{v_f B}/3\right) X^{-\frac{1}{3}} \left(2F(\zeta) - \zeta F'(\zeta)\right). \tag{5}$$

Now ζ is the dimensionless variable and $F(\zeta)$ and $\Theta(\zeta)$ are linear velocity field and temperature profile. Using similarity transformation, the above equations are:

$$3F''' + \lambda F''F'' - F'F' + 2FF'' \pm Gr\Theta + 1 - M\left(F' - 1\right) = 0, \tag{6}$$

$$\frac{1}{Pr}\left(1 + \frac{4}{3}Rd\right)\Theta'' + \frac{2}{3}F\Theta' + Ec\left(1 + \frac{\lambda}{2}F''\right)F''F'' + MF''F'' + Q\Theta = 0. \tag{7}$$

The boundary conditions are given by:

$$F(0) = 0,\ F'(0) = \gamma,\ \Theta(0) = 1 + \lambda_1\Theta'(0),\ F'(\infty) = 1,\ \Theta(\infty) = 0. \tag{8}$$

In above equations $\lambda = 3\Gamma\sqrt{\frac{2B^3}{v_f}}$ (Williamson parameter), $Pr = \frac{v_f}{\alpha_f}$ (Prandtl number). The physical quantities of engineering interest are defined as:

$$C_{fX} = \frac{\tau_{RX}}{\rho_f U_w^2},\ Nu_X = \frac{q_h}{k\left(T_w - T_\infty\right)},\ q_h = -k\left(1 + \frac{4}{3}Rd\right)\frac{\partial T}{\partial Y},\ \text{as } Y \to 0,$$
$$\tau_{RX} = \mu_f\left(\frac{\partial U}{\partial Y} + \frac{\Gamma}{\sqrt{2}}\frac{\partial U}{\partial Y}\frac{\partial U}{\partial Y}\right) \text{ as } Y \to 0. \tag{9}$$

Using equation (5) in equation (9) we get,

$$Re_X{}^{1/2}C_{fX} = F''(0) + \frac{\lambda}{6}F''(0)F''(0),\ Re_X^{-\frac{1}{2}}Nu_X = -\left(1 + \frac{4}{3}Rd\right)\Theta'(0). \tag{10}$$

The Reynolds number is Re_X.

3. Numerical procedure

Bvp4c is a MATLAB solver designed for Boundary Value Problems (BVPs) involving ordinary differential equations. It employs a collocation method based on the Lobatto IIIa formula, which provides a fourth-order accurate solution that is continuously differentiable over the specified interval. The solver adapts the computational mesh and controls error based on the residuals of the continuous solution. Users need to define the Ordinary Differential Equation (ODE) function, specify the boundary conditions, and provide an initial guess for both the solution and the mesh. The procedure of bvp4c method is presented in detail as below:

$$F = X(1);\ F' = X(2);\ F'' = X(3);\ F'' = XX1;\ \Theta = X(4);\ \Theta' = X(5);\ \Theta'' = XX2; \tag{11}$$

$$XX1 = \frac{-1}{3+\lambda X(3)}(-X(2)X(2)+2X(1)X(3)\pm GrX(5)+1-M(X(2)-1)); \tag{12}$$

$$XX2 = \frac{-1}{\frac{1}{Pr}\left(1+\frac{4}{3}Rd\right)}\left(\frac{2}{3}X(5)X(1)+Ec\left(1+\frac{\lambda}{2}X(3)\right)X(3)X(3)+MX(3)X(3)+QX(4)\right). \tag{13}$$

The appropriate conditions are:

$$X0(1) = 0;\ X0(2) = \gamma;\ X0(4) = 1+\lambda_1 X0(5);\ X\infty(2) = 1;\ X\infty(4) = 0; \tag{14}$$

4. Result and discussion

The developed dimensionless model have been through numerical technique bvp4c. The results of the involved parameters are presented through Figures 4-7 and numerical results through Table 1. Figure 4a discusses the variation of Williamson fluid factor and fluid velocity. The reduction in velocity is directly linked to the increase in the Williamson fluid factor. The Williamson fluid factor has risen. The viscoelastic effects associated with relaxation time have become stronger. This phenomenon has increased resistance to particle motion. The fluid motion along the stretching cylinder has slowed. Figure 4b depictes the impression of Grashof number on velocity. The increment in velocity is directly linked to the increase in the Grashof number. The velocity profile has increased with the Grashof number because rising thermal gradients have generated stronger buoyancy forces which caused the fluid to accelerate along the stretching surface. Figure 5a illustrates the effect of the MHD factor on velocity. The fluid velocity increased due to the enhancement of the magnetic field. The increase in the magnetic field strengthened the Lorentz force. The Lorentz force enhanced fluid motion in the Williamson fluid flow. The magnetic effect interacted with the fluid non-Newtonian properties. It reduced resistance near the sheet and increased the velocity.

Figures 5b-7 reported the effects of Ec (Eckert number), Pr (prandtl number), Q (heat generation), λ_1 (thermal slip) and Rd (radiation) on the temperature. Variation of Ec and temperature reported in Figure 5b. The temperature boosted up due to enrichment values of Ec. The temperature profile increased with higher Eckert numbers due to the more effective conversion of mechanical energy into heat. These conversion resulted in greater thermal energy accumulation leading to an increase in temperature. As the Eckert number increased the viscous dissipation effect became stronger. An increase in viscous dissipation resulted in a thicker thermal boundary layer in fluid phenomena. The influence of Pr on temperature

is illustrated in Figure 6a. The temperature gradually decreased as the value of *Pr* increased. A higher Prandtl number indicated lower thermal diffusivity compared to momentum diffusivity. This effect has reduced the thermal boundary layer thickness and limited heat penetration into the fluid. Thus, heat conduction away from the surface has weakened causing a sharper temperature drop near the surface. Figure 6b shows the variation of Q and temperature. The temperature increased due to the rise in Q. Internal heat increased the fluid thermal energy, which thickened the thermal boundary layer and raised the temperature distribution near the sheet. The generation of heat intensified both convective and conductive heat transfer mechanisms, which resulted in higher temperature values within the boundary layer. Figure 7a discussed the effect of λ_1 on temperature. The temperature curve shown lower values with higher levels of λ_1. Thermal slip reduced the efficiency of heat transfer at the fluid-solid interface. It limited thermal energy exchange by creating lower temperature gradient and resulted in a thinner thermal boundary layer. Temperature in the fluid near the surface decreased due to diminished thermal interaction. Figure 7b shows the relationship between *Rd* and temperature. The temperature profile rose with increasing levels of thermal radiation. Because thermal radiation added heat energy to the fluid and raised its temperature. This heat energy enhanced the thermal boundary layer thickness and physically caused an elevation in the temperature profile.

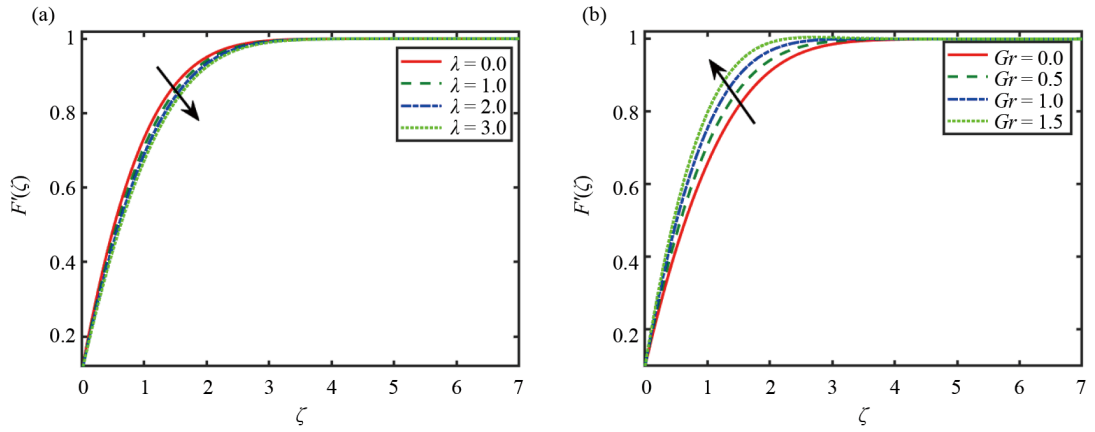


Figure 4. Impressions of λ and *Gr* on the velocity

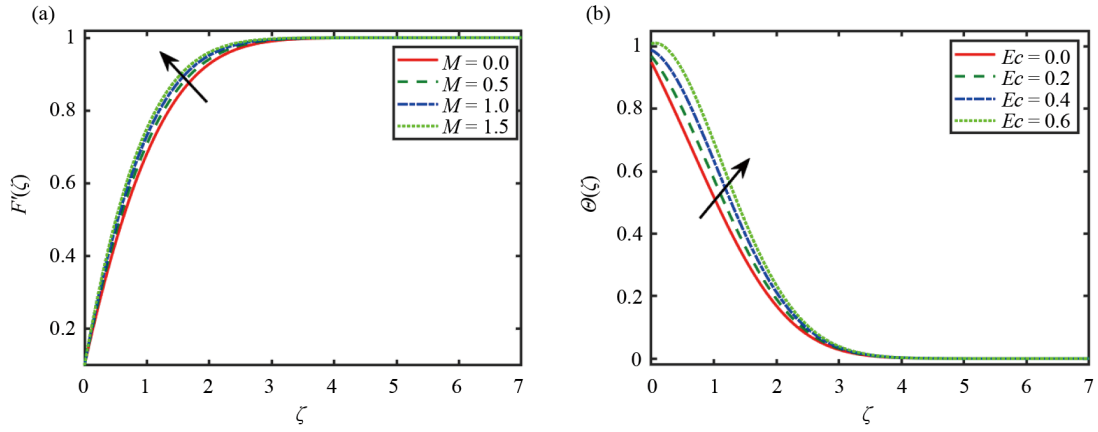


Figure 5. Impressions of *M* on the velocity and *Ec* on the Temperature

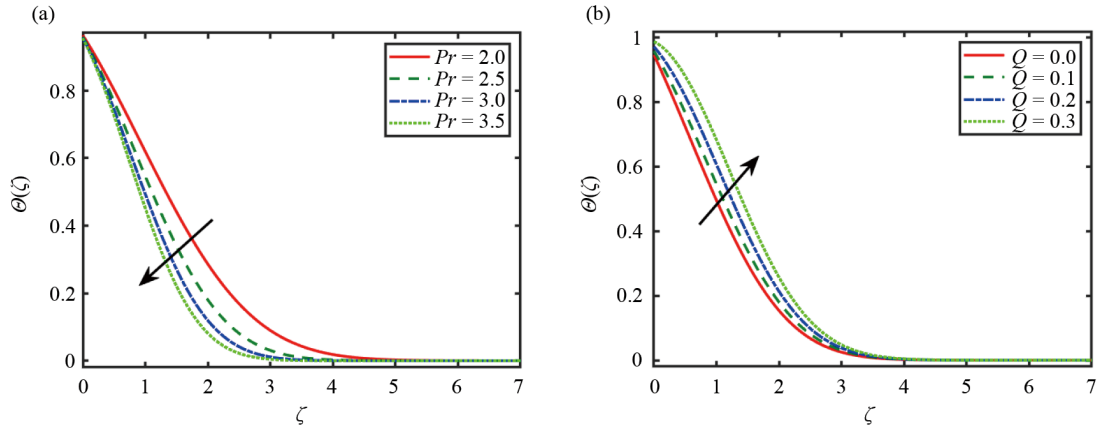


Figure 6. Impressions of Pr and Q on the temperature

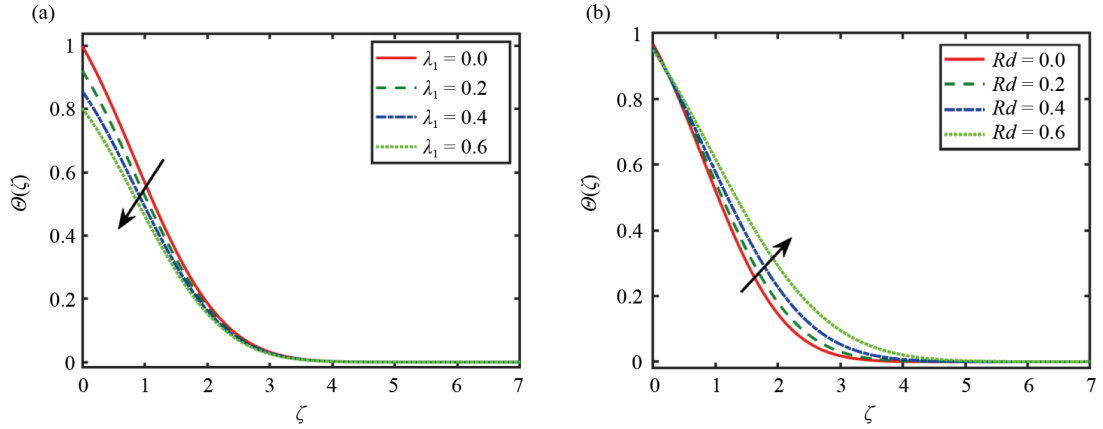


Figure 7. Impressions of λ_1 and Rd on the temperature

Table 1. Numerical impacts of physical factors on $Re_x^{-1/2}Nu_x$ and $Re_x^{1/2}C_{fx}$

M	λ	γ	Gr	Rd	Pr	Ec	λ_1	Q	$Re_x^{-1/2}Nu_x$	$Re_x^{1/2}C_{fx}$
0.0	1.0	0.1	0.5	0.2	2.5	0.2	0.1	0.1	0.37088936	0.86733429
0.5	-	-	-	-	-	-	-	-	0.31489848	0.95587550
1.0	-	-	-	-	-	-	-	-	0.25028557	1.03766740
1.5	-	-	-	-	-	-	-	-	0.17809066	1.11414070
0.5	0.0	-	-	-	-	-	-	-	0.34543523	0.91343393
-	1.0	-	-	-	-	-	-	-	0.31489848	0.95587550
-	2.0	-	-	-	-	-	-	-	0.29029897	0.99238807
-	3.0	-	-	-	-	-	-	-	0.26949361	1.02485250
-	1.0	0.0	-	-	-	-	-	-	0.23925622	1.03087300
-	-	0.1	-	-	-	-	-	-	0.31489848	0.95587550
-	-	0.2	-	-	-	-	-	-	0.38572887	0.87557335
-	-	0.3	-	-	-	-	-	-	0.45155429	0.79029729
-	-	0.1	0.0	-	-	-	-	-	0.32552315	0.83145485

Table 1. (cont.)

M	λ	γ	Gr	Rd	Pr	Ec	λ_1	Q	$Re_x^{-1/2}Nu_x$	$Re_x^{1/2}C_{fx}$
-	-	-	0.5	-	-	-	-	-	0.31489848	0.95587550
-	-	-	1.0	-	-	-	-	-	0.30066026	1.07746100
-	-	-	1.5	-	-	-	-	-	0.28319453	1.19707510
-	-	-	0.5	0.0	-	-	-	-	0.24936381	0.95281434
-	-	-	-	0.2	-	-	-	-	0.31489848	0.95587550
-	-	-	-	0.4	-	-	-	-	0.37456662	0.96005397
-	-	-	-	0.6	-	-	-	-	0.42174263	0.96614870
-	-	-	-	0.2	2.0	-	-	-	0.32386818	0.96673318
-	-	-	-	-	2.5	-	-	-	0.31489848	0.9558755
-	-	-	-	-	3.0	-	-	-	0.3072654	0.94942476
-	-	-	-	-	3.5	-	-	-	0.29020944	0.94505446
-	-	-	-	-	2.5	0.0	-	-	0.50630081	0.94691077
-	-	-	-	-	-	0.2	-	-	0.31489848	0.9558755
-	-	-	-	-	-	0.4	-	-	0.11815182	0.96497866
-	-	-	-	-	-	0.6	-	-	0.084103863	0.97422442
-	-	-	-	-	-	0.2	0.0	-	0.331363000	0.95964449
-	-	-	-	-	-	-	0.1	-	0.31489848	0.9558755
-	-	-	-	-	-	-	0.2	-	0.30001651	0.952459560
-	-	-	-	-	-	-	0.3	-	0.28649657	0.94934858
-	-	-	-	-	-	-	0.1	0.0	0.436823040	0.94821442
-	-	-	-	-	-	-	-	0.1	0.31489848	0.9558755
-	-	-	-	-	-	-	-	0.2	0.17344468	0.9651588
-	-	-	-	-	-	-	-	0.3	0.005232366	0.97669146

Table 1 discussed the influence of physical factors on the Nusselt number and skin friction. The increase in the magnetic field factor reduced the heat transfer factor and raised the friction at the surface. Lorentz force opposed fluid motion and reduced thinning of the thermal boundary layer which declined the heat transfer rate as the Nusselt number declined. Because the magnetic field induced a Lorentz force opposing fluid motion. The magnetic damping reduced velocity near the sheet and increased shear stress and skin friction at the surface. The magnetic field acts as additional drag and enhanced skin friction due to electromagnetic force resisting fluid flow. Heat transfer decreased, and surface friction increased due to the enrichment of the Williamson factor. The decrease in Nusselt number with increasing Williamson fluid parameter occurred because a higher Williamson factor increased shear thinning effects. A thicker thermal boundary layer suppressed thermal diffusion which consequently lowered the heat transfer rate. The skin friction increased with the Williamson fluid factor due to the higher fluid elasticity which enhanced resistance to flow near the stretching sheet. Consequently, the increased shear stress at the wall significantly raised the skin friction. The heat transfer increased while the skin friction decreased due to the elevated values of the stretching rate parameter. The stronger stretching intensified fluid motion and thinned the thermal boundary layer, significantly improving thermal performance. Skin friction decreased as the stretching rate parameter increased because stronger stretching accelerated fluid motion and reduced the velocity gradients at the surface. It led to decreased shear stress and improved overall flow smoothness. Heat transfer declined and friction became high due to enrichment in the Grashof factor. As the Grashof factor increased and the strength of buoyancy-driven flow intensified which enhanced fluid motion near the surface. The increase in the Grashof factor resulted in a steeper velocity gradient at the wall which in turn raised the skin friction coefficient and led to greater shear stress on the surface. Stronger convection typically results in a thicker thermal boundary layer which in turn decreases the temperature gradient at the wall. Both heat transfer and skin friction become high due to enlarging values of thermal radiation. Enhanced radiation energy increased temperature gradients as well as promoted stronger thermal diffusion and elevated the overall thermal performance of the system. Skin friction increased with higher thermal radiation because

intensified radiative heat transfer raised fluid temperature, which reduced viscosity and enhanced velocity gradients near the surface. This phenomenon led to greater shear stress at the wall which affected the momentum transfer and overall thermal performance. Both heat transfer and skin friction became low due to enlarging values of Prandtl number. Because higher Prandtl number indicated lower thermal diffusivity. The fluid motion is suppressed which led to weakened velocity gradients near wall. This phenomenon reduced surface shear stress and enhanced flow stability and control. Heat transfer declined and friction became high due to enrichment in Eckert number. Both heat transfer and surface friction decreased with higher thermal slip factor. Heat transfer declined and friction became high due to enrichment in heat generation factor. That decline associated with increasing heat generation parameter indicated a reduction in the thermal performance of Williamson fluid. As more heat is generated within the fluid as well as temperature gradient decreases. This weakening of the convective heat transfer led to a reduction in the Nusselt number. The internal heat production increased the thermal energy in the Williamson fluid, which resulted in a reduction of its viscosity near the stretching surface. This reduction intensified momentum transfer and velocity gradients at the wall, which led to higher shear stress. The comparative results presented in Table 2 indicate that the Boundary Value Problem Code (BVPC) and Numerical Differentiation (ND)-Solver methods produce very similar outcomes for both skin friction and the Nusselt number across all tested parameter values, with only slight variations noted in the fourth decimal place. Table 3 presents fourteen scenarios (S-1 to S-14), each comprising three cases (C-1, C-2, and C-3), designed to systematically vary the associated physical parameters.

Table 2. Competitive results with numerical (bvp4c) and ND solver method

M	Pr	BVP4C		ND-Solver	
		$Re_X^{-1/2}Nu_X$	$Re_X^{1/2}C_{fX}$	$Re_X^{-1/2}Nu_X$	$Re_X^{1/2}C_{fX}$
0.0	2.5	0.37088936	0.86733429	0.371889245	0.868334258
0.5	-	0.31489848	0.95587550	0.315898351	0.954875149
1.0	-	0.25028557	1.03766740	0.251285153	1.036667351
1.5	-	0.17809066	1.11414070	0.179091142	1.113141759
0.5	2.0	0.32386818	0.96673318	0.324868159	0.967733456
-	2.5	0.31489848	0.9558755	0.315898357	0.956875253
-	3.0	0.3072654	0.94942476	0.308265639	0.950425451
-	3.5	0.29020944	0.94505446	0.291209412	0.946054543
-	2.5	0.50630081	0.94691077	0.507301251	0.947911254

Table 3. Visualization of nine schemes for each of three cases

Schemes	Cases	M	λ	Gr	Rd	Pr	Ec	γ	λ_1	Q
Scheme-1	Case-1	0.0	1.0	0.5	0.2	2.5	0.2	0.1	0.1	0.1
-	Case-2	0.5	-	-	-	-	-	-	-	-
-	Case-3	1.0	-	-	-	-	-	-	-	-
Scheme-2	Case-1	0.5	0.0	-	-	-	-	-	-	-
-	Case-2	-	1.0	-	-	-	-	-	-	-
-	Case-3	-	2.0	-	-	-	-	-	-	-
Scheme-3	Case-1	-	1.0	0.0	-	-	-	-	-	-
-	Case-2	-	-	0.5	-	-	-	-	-	-
-	Case-3	-	-	1.0		-	-	-	-	-
Scheme-4	Case-1	-	-	0.5	0.0	-	-	-	-	-
-	Case-2	-	-	-	0.2	-	-	-	-	-
-	Case-3	-	-	-	0.4		-	-	-	-

Table 3. (cont.)

Schemes	Cases	M	λ	Gr	Rd	Pr	Ec	γ	λ_1	Q
Scheme-5	Case-1	-	-	-	0.2	2.0	-	-	-	-
-	Case-2	-	-	-	-	2.5	-	-	-	-
-	Case-3	-	-	-	-	3.0	-	-	-	-
Scheme-6	Case-1	-	-	-	-	2.5	0.0	-	-	-
-	Case-2	-	-	-	-	-	0.2	-	-	-
-	Case-3	-	-	-	-	-	0.4	-	-	-
Scheme-7	Case-1	-	-	-	-	-	0.2	0.0	-	-
-	Case-2		-	-	-	-	-	0.1	-	-
-	Case-3		-	-	-	-	-	0.2	-	-
Scheme-8	Case-1		-	-	-	-	-	0.1	0.0	-
-	Case-2	-	-	-	-	-	-	-	0.1	-
-	Case-3	-	-	-	-	-	-	-	0.2	-
Scheme-9	Case-1	-	-	-	-	-	-	-	0.1	0.0
-	Case-2	-	-	-	-	-	-	-	-	0.1
-	Case-3	-	-	-	-	-	-	-	-	0.2

5. NNA

The NNA approach is developed as alternative to traditional mathematical models for evaluating model accuracy. Due to their advanced systematic capabilities, the NNA model served as effective engineering tool even for simulating complex system that lack clear functional relationships. Figure 2 illustrates a single neuron withnodes as input. The neural network architecture is created and trained using MATLAB specifically utilizing the feed forward technique with one hidden layer and employing LMS training method. The table consists of nine schemes, and it presents three cases, each concentrating on a specific parameter such as the Magnetic parameter (M), Williamson fluid parameter (λ), stretching parameter (γ), Grashof factor (Gr), Radiation factor (Rd), Prandtl number (Pr), Eckert number (Ec), Thermal slip (λ_1), and heat generation (Q). Table 4 presented the results of training a ANN for each case within all nine schemes. Scheme 1 achieved balanced performance across all cases with nearly identical error magnitudes with confirming stable learning behavior. Scheme 2 showed faster convergence low epochs and the smallest gradient 9.1622×10^{-8}. All the cases maintained low and uniform errors. Scheme 3 produced minimal training and testing errors with moderate gradients, particularly stable in all cases. Scheme 4 converged rapidly with low gradient 9.55×10^{-8}. All cases are showing high computational efficiency. Scheme 5 demonstrated uniform convergence and smooth error distribution across cases. It indicated strong model stability and consistent accuracy. Scheme 6 retained acceptable error levels but exhibited higher gradients 2.5092×10^{-6}. Scheme 7 achieved lower testing errors 2.0573×10^{-8} with moderate gradients, confirming accurate and reliable convergence behavior. Scheme 8 yielded the smallest overall errors 1.85×10^{-8} and made it as the best performing. Scheme 9 displayed the fastest convergence and a minimal gradient 9.913×10^{-8}. It confirmed high learning efficiency with reliable accuracy across all cases. The results summarized in the Table 4 validate reliable and stable convergence across all schemes having training, validation and testing errors residual in the range of 10^{-8} which indicates excellent model accuracy and generalization.

Table 4. Results of TNN across three distinct cases involving nine schemes

Schemes	Cases	Training	Validation	Testing	Epoch	Performance	Gradient	Time
Scheme-1	Case-1	2.154e-08	2.0843e-08	2.2194e-08	100	2.154e-08	1.7156e-07	3.805
-	Case-2	2.3735e-08	2.1692e-08	2.1668e-08	100	2.3735e-08	9.3894e-07	3.835
-	Case-3	2.5107e-08	2.5175e-08	2.5317e-08	100	2.5107e-08	6.391e-07	3.776
Scheme-2	Case-1	2.4507e-08	2.4388e-08	2.3681e-08	60	2.4507e-08	9.1622e-08	2.243
-	Case-2	2.3002e-08	2.2086e-08	2.1337e-08	100	2.3002e-08	1.7911e-07	4.694
-	Case-3	2.105e-08	2.1274e-08	2.1678e-08	100	2.105e-08	2.5405e-07	5.046
Scheme-3	Case-1	2.0339e-08	2.0409e-08	2.0987e-08	100	2.0339e-08	1.1616e-06	3.961
	Case-2	2.2379e-08	2.1913e-08	2.3372e-08	100	2.2379e-08	8.6075e-07	4.123
	Case-3	2.4615e-08	2.641e-08	2.3215e-08	100	2.4615e-08	1.6426e-07	4.137
Scheme-4	Case-1	2.2998e-08	2.4032e-08	2.3564e-08	58	2.2998e-08	9.1598e-08	2.174
-	Case-2	2.3933e-08	2.237e-08	2.1394e-08	44	2.3933e-08	9.55e-08	1.708
-	Case-3	2.3746e-08	2.1531e-08	2.0662e-08	100	2.3746e-08	2.3672e-07	4.053
Scheme-5	Case-1	2.2595e-08	2.3161e-08	2.1341e-08	100	2.2595e-08	9.2653e-08	3.992
-	Case-2	2.4509e-08	2.1994e-08	2.1606e-08	100	2.4509e-08	4.7306e-07	4.200
-	Case-3	2.3164e-08	2.1194e-08	2.2263e-08	100	2.3164e-08	2.6158e-07	3.922
Scheme-6	Case-1	2.3514e-08	2.1467e-08	2.3167e-08	100	2.3514e-08	2.5092e-06	4.062
-	Case-2	2.1986e-08	2.3536e-08	2.3659e-08	100	2.1986e-08	5.116e-07	3.954
-	Case-3	2.3344e-08	2.2377e-08	2.2048e-08	100	2.3344e-08	3.3404e-07	4.041
Scheme-7	Case-1	2.4279e-08	2.2351e-08	2.0573e-08	100	2.4279e-08	1.6519e-07	3.923
-	Case-2	2.1443e-08	2.2495e-08	2.09e-08	100	2.1443e-08	2.1493e-07	4.091
-	Case-3	2.2356e-08	2.3121e-08	2.2765e-08	100	2.2348e-08	5.2644e-07	3.776
Scheme-8	Case-1	2.5938e-08	2.6335e-08	2.7829e-08	100	2.591e-08	6.9561e-07	3.73
-	Case-2	2.1037e-08	2.3071e-08	2.2697e-08	100	2.1037e-08	2.4934e-07	4.02
-	Case-3	1.8512e-08	1.8658e-08	1.8385e-08	100	1.8512e-08	3.1411e-07	3.843
Scheme-9	Case-1	2.3851e-08	2.4004e-08	2.2872e-08	43	2.3851e-08	9.913e-08	1.629
-	Case-2	2.1998e-08	2.183e-08	2.1497e-08	100	2.1998e-08	5.6971e-07	3.847
-	Case-3	2.315e-08	2.2927e-08	2.2239e-08	100	2.315e-08	4.4657e-07	3.788

Figure 8a-f illustrated the model fit to the output and the progression of training clearly demonstrating that the model effectively captured the fundamental patterns in the training data. The function fit to out with target values have great accuracy which presented in the Figure 8a, c, e. Figure 8b, d, f presented the training and validation of the results. Our results presented that the error of gradient range is 10^{-7} to 10^{-8}. From the figures, it is observed that the training and curve fitting processes minimized the error and achieved accurate convergence of the results. The regression analysis and validation performance are evaluated as shown in Figure 9a-f. The approach included partitioning the dataset into training and validation portions which used the training set for model fitting and testing its predictive capability on the validation set. Common metrics used for the assessment include the Root Mean Squared Error (RMSE), Mean Squared Error (MSE), Mean Absolute Error (MAE) and the coefficient of determination R^2 with lower error values and higher R^2 indicating better model performance. Validation and residual plots reveal model generalization and highlight overfitting when validation performance accuracy. This process is essential for selecting a model that effectively fits training data while ensuring strong generalization and robust having reliable predictive performance. Figure 10 provide a comparative analysis of predictions made by ANN and the numerical results. These figures demonstrate that the ANN model closely matches the numerical solutions, validating the accuracy of the ANN approach. Figure 11 compare the stream function distributions for Newtonian and non-Newtonian fluid. The results highlight significant differences in flow behavior between the two fluid models especially in terms of streamline patterns. These figures emphasize the effectiveness of ANN modeling and illustrate the distinct flow characteristics of Newtonian versus non-Newtonian fluid.

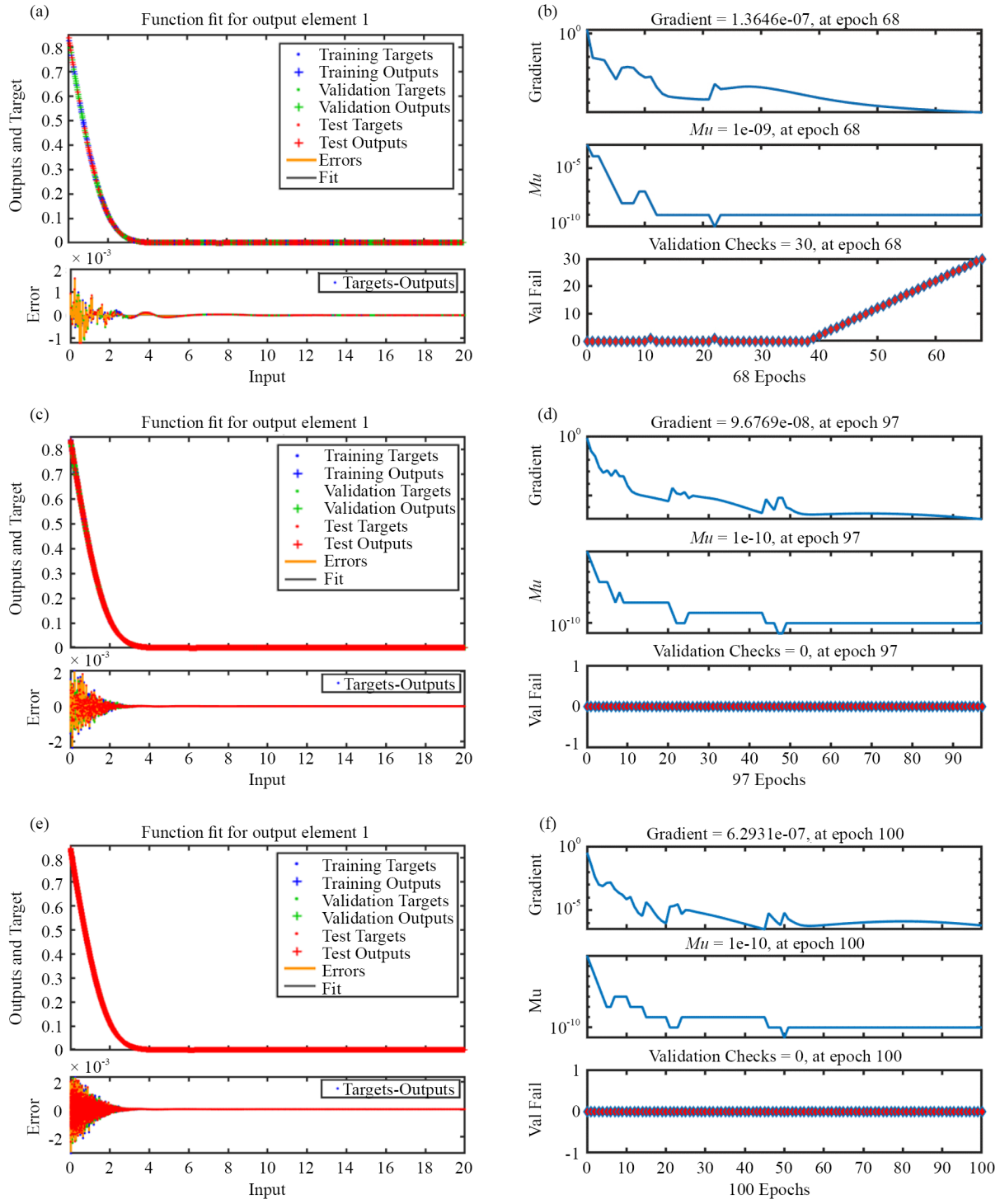


Figure 8. Analysis of fit for output and Training of current model

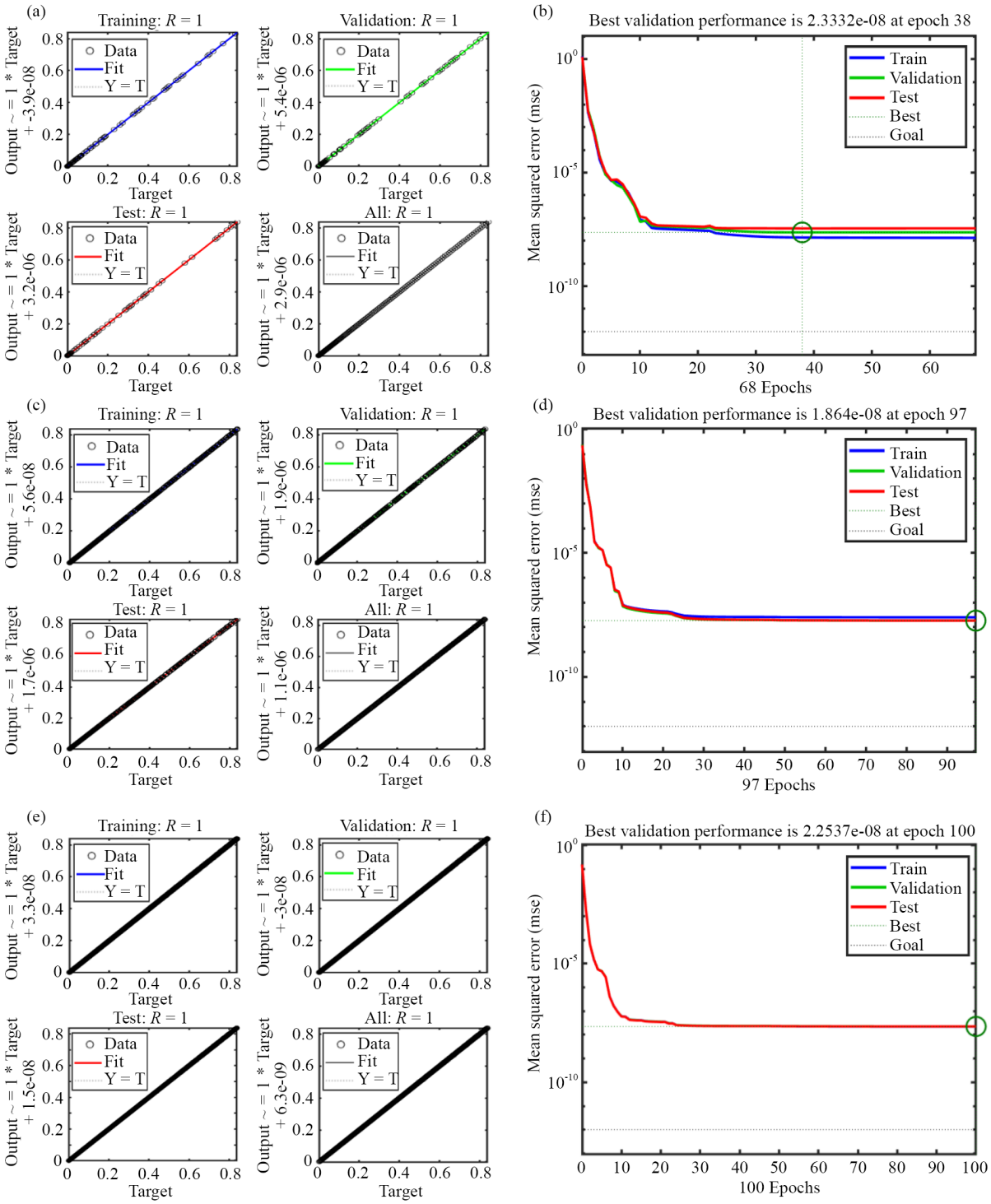


Figure 9. Regression analysis and Validation performace of current model

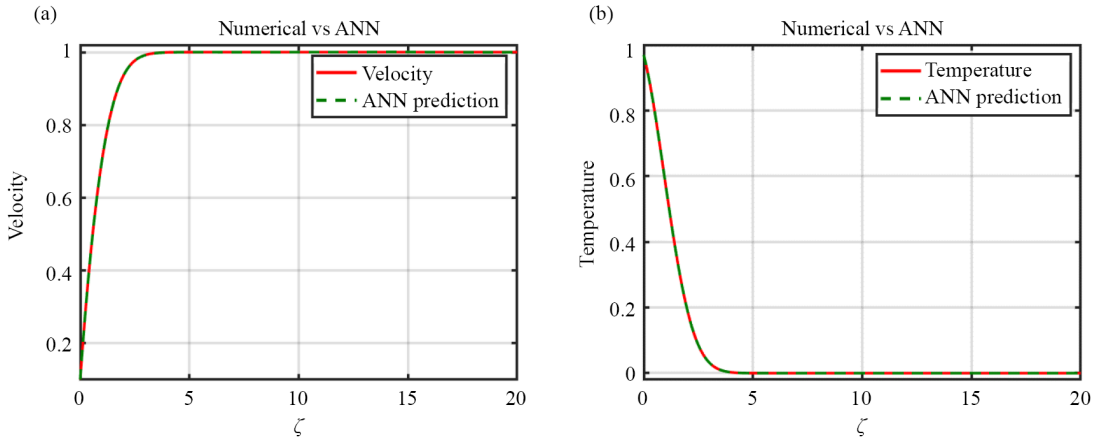


Figure 10. Comparative results of ANN with numerical for velocity and Temperature

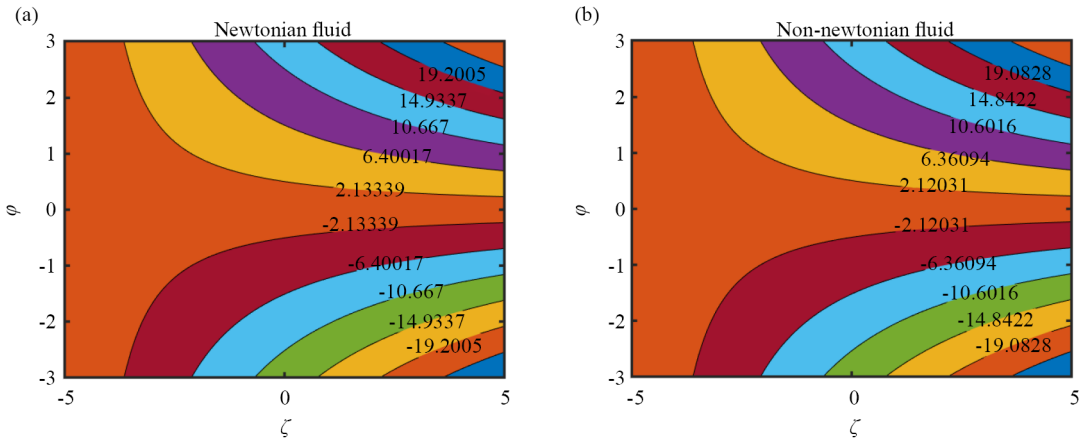


Figure 11. Stream function for Newtonian and non Newtonian fluid

6. Response Surface Methodology (RSM)

RSM is used to analyze the relationship among input factors and output responses in order to formulate the perfect correlation between them. This section contains the RSM for output response Nusselt number and input factors, *Pr*, *Rd* and *Ec*. Further, Analysis of Variance (ANOVA) and sensitivity of output response is presented in detail. The general expression signifying relationship of output response Nusselt number (Nu) and input parameters *A*, *B* and *C* can be defined as following

$$Nu = \Gamma_0 + \Gamma_1 A + \Gamma_2 B + \Gamma_3 C + \Gamma_4 AB + \Gamma_5 AC + \Gamma_6 BC + \Gamma_7 A^2 + \Gamma_8 B^2 + \Gamma_9 C^2. \tag{15}$$

Where Γ_i, $i = 0, 1, \ldots, 9$ indicates unknown constants called the regression coefficients. These regression coefficients will be determined with the help of RSM. The levels of parameters *Pr*, *Rd* and *Ec* at low (-1), medium (0), and high (+1) relevant position are tabulated in Table 5.

Table 5. Symbolic representation of input factors with specific levels and values

Parameters	Symbol	Levels		
		-1 (low)	0 (medium)	1 (high)
Pr	A	2.5	3.0	3.5
Rd	B	0.2	0.4	0.6
Ec	C	0.1	0.2	0.3

Twenty runs and nineteen degrees of freedom relevant to above selected parameters are required by RSM to run successfully. These are presented in Table 6.

Table 6. Experiment design with coded and actual estimations of parameters

Experiment number	Coded values			Real values			Response
	A	B	C	*Pr*	*Rd*	*Ec*	*Nu*
1	-1	-1	-1	2.5	0.2	0.1	0.4112577
2	1	-1	-1	3.5	0.2	0.1	0.45111658
3	-1	1	-1	2.5	0.6	0.1	0.50391892
4	1	1	-1	3.5	0.6	0.1	0.60427081
5	-1	-1	1	2.5	0.2	0.3	0.21720331
6	1	-1	1	3.5	0.2	0.3	0.12623815
7	-1	1	1	2.5	0.6	0.3	0.33867969
8	1	1	1	3.5	0.6	0.3	0.24861767
9	-1	0	0	2.5	0.4	0.2	0.37456662
10	1	0	0	3.5	0.4	0.2	0.35906488
11	0	-1	0	3.0	0.2	0.2	0.3072654
12	0	1	0	3.0	0.6	0.2	0.43841453
13	0	0	-1	3.0	0.4	0.1	0.50850449
14	0	0	1	3.0	0.4	0.3	0.23863608
15	0	0	0	3.0	0.4	0.2	0.37462925
16	0	0	0	3.0	0.4	0.2	0.37462925
17	0	0	0	3.0	0.4	0.2	0.37462925
18	0	0	0	3.0	0.4	0.2	0.37462925
19	0	0	0	3.0	0.4	0.2	0.37462925
20	0	0	0	3.0	0.4	0.2	0.37462925

7. ANOVA

Analysis of variance (ANOVA) is crucial to determine variance to obtain significant correlations between input parameters. The regression coefficients given in equation (15) are obtained with the help of MINITAB software. Table 7 and Table 8 show all of the statistical estimations using the ANOVA.

Table 7. ANOVA for Nusselt number Nu

Source	DF	Adj SS	Adj MS	F-value	P-value
Model	9	0.224350	0.024928	474.24	0.000
Linear	3	0.210389	0.070130	1,334.20	0.000
A	1	0.000317	0.000317	6.03	0.034
B	1	0.038542	0.038542	733.25	0.000
C	1	0.171530	0.171530	3,263.30	0.000
Square	3	0.000590	0.000197	3.74	0.049
$A*A$	1	0.000189	0.000189	3.59	0.087
$B*B$	1	0.000014	0.000014	0.27	0.616
$C*C$	1	0.000006	0.000006	0.12	0.733
2-way interaction	3	0.013371	0.004457	84.79	0.000
$A*B$	1	0.000471	0.000471	8.96	0.013
$A*C$	1	0.012899	0.012899	245.40	0.000
$B*C$	1	0.000000	0.000000	0.01	0.926
Error	10	0.000526	0.000053		
Lack-of-fit	5	0.000526	0.000105	*	*
Pure error	5	0.000000	0.000000		
Total	19	0.224876			

Table 8. Regression coefficients for response Nu

Term	Coeficient	P-value	Significant
Constant	0.37482	0.000	Yes
A	-0.00563	0.034	Yes
B	0.06208	0.000	Yes
C	-0.13097	0.000	Yes
$A*A$	-0.00829	0.087	No
$B*B$	-0.00226	0.616	No
$C*C$	-0.00153	0.733	No
$A*B$	0.00767	0.013	Yes
$A*C$	-0.04015	0.000	Yes
$B*C$	-0.00024	0.926	No
$R^2 = 99.77\%$		Adj $R^2 = 99.56\%$	

Equation (15) can be assessed based on its P-value. The P-value is helpful for validation of regression models. In statically sense, the P-value smaller than 0.05 is important and the P-value bigger than 0.05 will be ignored. It is noted that the square terms, A^2, B^2 and C^2 are BC not significant based on respective P-values mentioned in Table 8. Ultimately, mathematical equation (15) will take the form

$$Nu = 0.37482 - 0.00563A + 0.06208B - 0.13097C + 0.00767AB - 0.04015AC. \tag{16}$$

Present model shows goodness of fit. The reason for that is the coefficient of determination for Nu is 99.77% as given in Table 8 which shows the accuracy of the model. Different error graphs are also sketched in Figure 12 to validate

the authenticity of current analysis. The normality, independence and randomness assumptions of ANOVA is confirmed by residual plots.

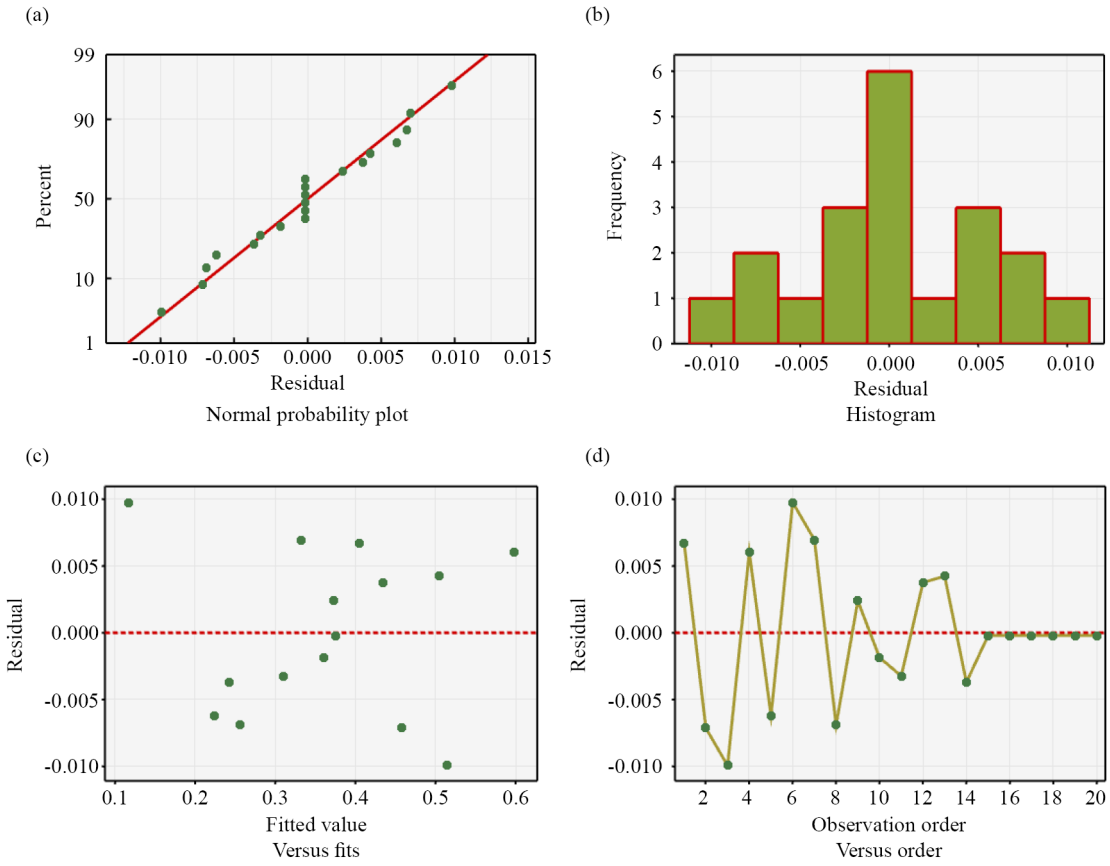


Figure 12. Residual plots for Nusselt number

8. Sensitivity analysis

The sensitivity analysis is extensively utilized technique in various scientific disciplines in order to examine how the inputs can be allocated to the responses (outputs) in a physically important procedure. It is used to check the efficiency of responses within a system. In the problem under consideration, the sensitivity of the Nu in relation with input factors A, B and C is scrutinized. By using equation (16), the sensitivity function of output response (Nu) can be written as

$$\frac{\partial Nu}{\partial A} = -0.00563 + 0.00767B - 0.04015C. \tag{17}$$

$$\frac{\partial Nu}{\partial B} = 0.06208 + 0.00767A. \tag{18}$$

$$\frac{\partial Nu}{\partial C} = -0.13097 - 0.04015C. \tag{19}$$

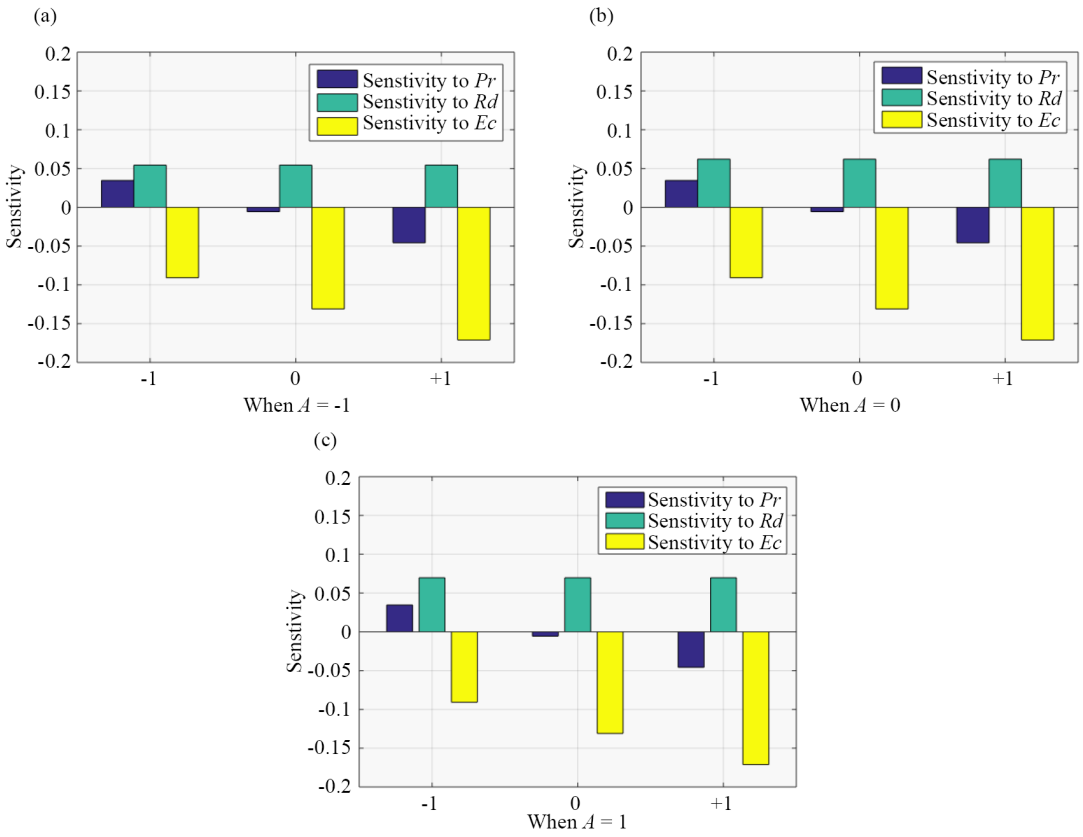


Figure 13. Sensitivity plots for output Nu by keeping $B = 0$

The bar charts of sensitivity of response corresponding to inputs are prepared and presented the in Figure 13a-c to get clear understanding. The response augments if bar chart grows in positive direction whereas the response lowers if the bar chart shows negative manner. The enhancement of the height of bar chart expresses that the responses are more sensitive to the input parameters. In this analysis, the computed sensitivities of the output (Nu) to the input influencing variables (Pr, Rd, Ec) for all levels (low, medium, and high). The sensitivity of Nu related to parameter Rd is positive for all levels while the negative sensitivity of Nu is noticed for factors Ec. Sensitivity of Pr is showing mix behavior as it is positive at lower level while it is negative at medium and higher levels. It shows that the sensitivity of Nu has a direct relation with Rd signifying that the sensitivity of Nu rises when this parameter rises. In contrast, the sensitivity of Nu become lower when factors is higher. It is found that response Nu is most sensitive to factor Ec because the height of bar chart for this factor is largest as compared to Pr and Rd.

9. Conclusions

We focus on the flow of Williamson fluid over a vertical variable stretching surface, considering both viscous dissipation and heat generation. The governing equations (ODE's) are solved using numerical techniques. ANN were employed as robust predictive tool for modeling the system behavior. The integration of ANN demonstrated its effectiveness in accurately estimating velocity and temperature profiles based on key physical parameters. The combined approach emphasized the potential of ANN to function as contemporary computational tool for addressing complex fluid dynamics issues. Response surface methodology is taken into account to find correlation between input parameter and

output response. Based on the technique, ANOVA is presented and residual errors are plotted to validate. Sensitivity analysis of input parameter on output response is determined by calculating unknown regression coefficients. The key features of our analysis are as follows:

• The fluid velocity increased due to the enhancement of the magnetic field. The increase in the magnetic field strengthened the Lorentz force. The Lorentz force enhanced fluid motion in the Williamson fluid flow and increased the velocity.

• The temperature boosted up due to enrichment values of Ec. The temperature profile increased with higher Eckert numbers due to the more effective conversion of mechanical energy into heat.

• A higher Prandtl number indicated lower thermal diffusivity compared to momentum diffusivity. Heat conduction away from the surface has weakened causing a sharper temperature drop near the surface.

• The temperature profile rose with increasing levels of thermal radiation. Because thermal radiation added heat energy to the fluid and raised its temperature.

• The neural network effectively learns and generalizes physical phenomena, with declining MSE trends and efficient optimization dynamics.

• Stable gradient reduction and adaptive learning rate decay ensure precise and robust training, with potential improvements in handling overfitting.

• Future work: Extend the analysis to unsteady and three-dimensional flows over vertical variable stretching surfaces in the presence of MHD and stagnation point effects. Investigate the influence of additional non-Newtonian models and complex boundary conditions, such as porous or permeable surfaces on Williamson fluid dynamics.

Availability of data and materials

The data and material are available and can be shared upon request.

Funding

No funding was received for preparing this research article.

Acknowledgement

The authors would like to thank Prince Sultan University for their support through the TAS research lab.

Conflict of interest

The authors declare that they have no known competing financial interests or personal relationships that could have appeared to influence the work reported in this paper.

References

[1] Sakiadis BC. Boundary-layer behavior on continuous solid surfaces: I. Boundary-layer equations for two-dimensional and axisymmetric flow. *AIChE Journal*. 1961; 7(1): 26-28.

[2] Crane LJ. Flow past a stretching plate. *Zeitschrift für Angewandte Mathematik und Physik*. 1970; 21(4): 645-647.

[3] Mahapatra TR, Gupta AS. Stagnation-point flow towards a stretching surface. *Canadian Journal of Chemical Engineering*. 2003; 81(2): 258-263.

[4] Sharma PR, Sinha S, Yadav RS, Filippov AN. MHD mixed convective stagnation point flow along a vertical stretching sheet with heat source/sink. *International Journal of Heat and Mass Transfer*. 2018; 117: 780-786.
[5] Mahmood Z, Alhazmi SE, Alhowaity A, Marzouki R, Al-Ansari N, Khan U. MHD mixed convective stagnation point flow of nanofluid past a permeable stretching sheet with nanoparticles aggregation and thermal stratification. *Scientific Reports*. 2022; 12(1): 16020.
[6] Abbas N, Ul Huda N, Shatanawi W, Mustafa Z. Melting heat transfer of Maxwell-Sutterby fluid over a stretching sheet with stagnation region and induced magnetic field. *Modern Physics Letters B*. 2024; 38(15): 2450085.
[7] Sohail M, Ali MH, Abodayeh K, Abbas ST. Bio-convective boundary layer flow of Maxwell nanofluid via optimal homotopic procedure with radiation and Darcy-Forchheimer impacts over a stretched sheet. *International Journal of Ambient Energy*. 2025; 46(1): 2462583.
[8] Salahuddin T, Malik MY, Hussain A, Bilal S, Awais M. MHD flow of Cattanneo-Christov heat flux model for Williamson fluid over a stretching sheet with variable thickness: Using numerical approach. *Journal of Magnetism and Magnetic Materials*. 2016; 401: 991-997.
[9] Hamid A, Khan M, Hafeez A. Unsteady stagnation-point flow of Williamson fluid generated by stretching/shrinking sheet with Ohmic heating. *International Journal of Heat and Mass Transfer*. 2018; 126: 933-940.
[10] Megahed AM. Williamson fluid flow due to a nonlinearly stretching sheet with viscous dissipation and thermal radiation. *Journal of the Egyptian Mathematical Society*. 2019; 27(1): 12.
[11] Wang F, Asjad MI, Rehman SU, Ali B, Hussain S, Gia TN, et al. MHD Williamson nanofluid flow over a slender elastic sheet of irregular thickness in the presence of bioconvection. *Nanomaterials*. 2021; 11(9): 2297.
[12] Botmart T, Sabir Z, Raja MAZ, Sadat R, Ali MR. Stochastic procedures to solve the nonlinear mass and heat transfer model of Williamson nanofluid past over a stretching sheet. *Annals of Nuclear Energy*. 2023; 181: 109564.
[13] Geetha R, Reddappa B, Tarakaramu N, Rushi Kumar B, Ijaz Khan M. Effect of double stratification on MHD Williamson boundary layer flow and heat transfer across a shrinking/stretching sheet immersed in a porous medium. *International Journal of Chemical Engineering*. 2024; 2024(1): 9983489.
[14] Ahsan N, Alhowaity A, Abdelmohimen MA, Alrihieli HF, Al-Mdallal QM. Insights of thermal behavior of bioconvective Williamson fluid flow over a porous curved stretching surface with chemical reactions: A numerical study. *Case Studies in Thermal Engineering*. 2025; 68: 105924.
[15] Ishak A, Jafar K, Nazar R, Pop I. MHD stagnation point flow towards a stretching sheet. *Physica A: Statistical Mechanics and Its Applications*. 2009; 388(17): 3377-3383.
[16] Mishra A, Rawat SK, Yaseen M, Pant M. Development of machine learning algorithm for assessment of heat transfer of ternary hybrid nanofluid flow towards three different geometries: Case of artificial neural network. *Heliyon*. 2023; 9(11): e21453.
[17] Nadeem S, Arif M, Ullah I, Alzabut J. MHD natural convection of nanofluid flow using a corrugated permeable medium within corrugated circular cavity. *Journal of Thermal Analysis and Calorimetry*. 2025; 150: 5697-5724.
[18] Vajravelu K, Hadjinicolaou A. Heat transfer in a viscous fluid over a stretching sheet with viscous dissipation and internal heat generation. *International Communications in Heat and Mass Transfer*. 1993; 20(3): 417-430.
[19] Shafiq A, Çolak AB, Sindhu TN, Al-Mdallal QM, Abdeljawad T. Estimation of unsteady hydromagnetic Williamson fluid flow in a radiative surface through numerical and artificial neural network modeling. *Scientific Reports*. 2021; 11(1): 14509.
[20] Madhu J, Baili J, Kumar RN, Prasannakumara BC, Gowda RJP. Multilayer neural networks for studying three-dimensional flow of non-Newtonian fluid flow with the impact of magnetic dipole and gyrotactic microorganisms. *Physica Scripta*. 2023; 98(11): 115228.
[21] Fatima N, Ghodhbani R, Khalid N, Khan MI, Taha T, Ijaz N, et al. Machine learning-based prediction of heat transfer enhancement in Carreau fluids with impact of homogeneous and heterogeneous reactions. *Multiscale and Multidisciplinary Modeling, Experiments and Design*. 2025; 8(2): 145.
[22] Shaheen A, Abbas N, Shatanawi W, Zil-e-Huma. Artificial neural network analysis of temperature-dependent properties of second-grade nanofluid flow over an exponentially curved Riga surface. *Modern Physics Letters B*. 2025; 39(32): 2550200.